X-Ray Photoelectron Spectroscopy of Metal & Metal-based Clusters: Au, Ag & Sn Cases.

LUND
UNIVERSITY

Master Thesis
60 Credits

Charles Wright

Supervisor: Prof. Stacey Ristinmaa Sörensen
Co-Supervisor: Dr. Maxim Tchapylguine

Division of Synchrotron Radiation Research
Department of Physics
June 2016

Abstract

Clusters are particles which consist of a finite number ($2 - 10^{6-7}$) of atoms/molecules. For the work presented in this thesis free clusters have been produced in order to study their properties, free of interfering substrates, using photoelectron spectroscopy at the MAX-lab synchrotron facility in Lund, Sweden. The clusters were produced using a magnetron-based sputtering source and are considered large enough for their properties to be adequately described using macroscopic descriptions.

Clusters of gold and silver have been produced and exposed to bromobenzene vapour in order to examine the adsorption of bromobenzene to the clusters. The approximate sizes of the clusters were determined using the liquid drop model and the fraction of their surface area to which bromobenzene adsorbed was estimated via the relative intensities of spectral components. Gold clusters were found to have a radius of $15 - 20$ Å and a coverage fraction of 0.58, while silver clusters were found to have a radius of $30 - 45$ Å and a coverage fraction of 0.76. The photoelectron experiments on free gold and silver clusters, picking up bromobenzene molecules, have allowed us to shed additional light on the details of bromobenzene adsorption; which is relevant to an important and sophisticated catalytic process.

Studies of free tin and tin oxide clusters were also conducted and the chemical shift of the $4d$ level between metallic tin and tin (IV) oxide was found to be $\approx 4.2\ eV$, not the $2.0\ eV$ previously reported[1]. Using the liquid drop model the size of metallic tin clusters was found to be $\approx 3 - 5\ nm$. The tin oxide clusters have also been deposited on a silicon substrate. The results of x-ray photoelectron studies conducted on these deposited clusters of metallic tin, tin (II) oxide and tin (IV) oxide are consistent with those conducted on free clusters. Size estimation via SEM images found deposited tin (II) oxide and tin (IV) oxide clusters to have radii of approximately $10\ nm$ and $10 - 20nm$ respectively. The possibility to create nanoscale tin oxide of controlled composition is important for the current activities in the field of large-gap transparent semiconductors.

Acknowledgements

This thesis could not have been completed without the aid of others. Firstly I would like to thanks my supervisors Prof. Stacey Sörensen (Head of the division of synchrotron radiation research and Pro vice-chancellor at Lund University) and Dr. Maxim Tchaplyguine (Beamline Manager at the MAX IV Laboratory) for their guidance and support throughout the period of writing.

I would also like to express my gratitude to other supporting members from the division of synchrotron radiation research. Joachim Schnadt provided the raw data concerning gold clusters, silver clusters and bromobenzene vapour; and Erik Mårcell, supervised by Prof Anders Mikkelsen, provided the SEM images of tin oxide clusters.

My own participation involved conducting the experiments on tin and tin oxide clusters, under direction by Maxim Tchaplyguine, in addition to the data analysis for all experiments and the subsequent discussion.

Contents

Abbreviations

SEM Scanning electron microscopy

PES Photoelectron spectroscopy

XPS X-ray photoelectron spectroscopy

LDM Liquid drop model

1 Introduction

1.1 Clusters

Clusters are nanoparticles which consist of a finite number of atoms or molecules. Though there is still debate as to their exact size, $2 - 10^{6-7}$ particles has been suggested[2]. They have properties between those of individual atoms/molecules where each atom is significant and those of bulk materials[3]. These properties are size-related and depend upon the number of atoms in the cluster and upon their geometric structure. For small clusters the addition of a single atom can dramatically alter their properties, i.e. the clusters properties do not evolve smoothly with the addition of component atoms/molecules. For large clusters however their properties evolve smoothly with cluster size[4]. This behaviour is illustrated in fig 1.

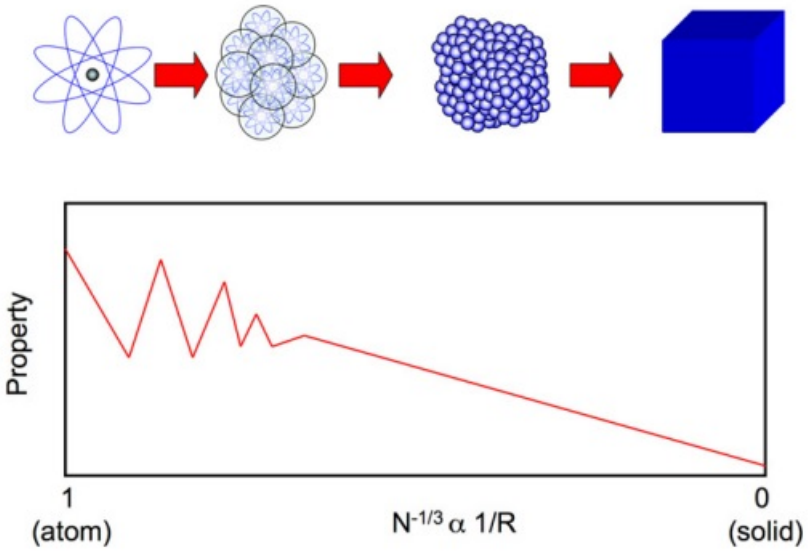

Figure 1: Taken from "Free clusters studied by core-level spectroscopies"[5]. This progression is erratic for small clusters but becomes smooth for larger clusters. For very large clusters the properties become identical to those of the bulk material. N refers to the number of particles and R to the cluster radius.

This smooth development of properties for larger clusters gives rise to so-called scaling laws[2], which allow for prediction of a cluster's properties given its size or for its size to be determined from its measured properties. An example of these scaling laws is provided by the Liquid Drop Model (LDM). This is the simplest model for metal clusters and arises from classical electrostatics[2].

$$WF(R) = WF_\infty + \frac{3}{8}\frac{1}{4\pi\sigma_0 R} \tag{1}$$

$$WF(R) = WF_\infty + \frac{5.40}{R(\text{Å})}eV \tag{2}$$

Equation 1 arises from this model and describes how the work-function for metal clusters decreases as cluster size increases, showing a linear dependence on the inverse of a cluster's radius. In these equations WF_∞ is the polycrystalline bulk work function, σ_0

is the permittivity of free space, R is the radius of the cluster and $WF(R)$ is the WF at the given radius. Equation 2 is equation 1 given in units of electron volts and Ångstroms as electron volts are the units typically used in photoelectron experiments, making this equation easier to work with.

Clusters have many applications in technology, both realised and potential. These applications may depend on the unique properties of clusters or upon their much greater surface area to volume ratio with regards to the bulk material. The high surface area to volume ratio of clusters is of interest in the field of catalysis, as they provide many activation sites while using only a little of the required material. Since deposition on a substrate would affect the electronic energy levels of the clusters and may alter their geometry, it is necessary to study free clusters in order to completely understand how their inherent properties develop with size.

This thesis revolves around two investigations of free clusters: the potential use of gold and silver clusters in specific catalytic applications and the accurate determination of specific oxide states of tin.

1.2 Motivation for Gold and Silver Studies

Bromobenzene (C_6H_5Br) is a volatile organic chemical consisting of one bromine atom bonded to a phenyl group. It is produced in large quantities during the incineration of waste printed circuit boards and due to its toxicity there has been a political movement to develop catalytic processes which would mitigate this hazard.

One of these processes could be cross-coupling reactions. These are a broad class of reactions in which organic halides, such as the aryl halide bromobenzene, and organometallic reagents are catalysed by metals and couple to form a third molecule with new carbon-carbon bonds[6]. It has been found that metal catalyst promoted C-C coupling reactions involving iodobenzene, another aryl halide, occur on Ag(111) and Au(111) surfaces and result in biphenyl desorption[7] [8]. Additionally kinetic and theoretical studies,[9] as well as studies in vacuo,[10] have shown extended gold surfaces to be suitable for a specific type of cross-coupling reaction known as Sonogashira cross-coupling involving the aryl halide iodobenzene.

Bromobenzene interacting with gold nanoparticle catalysts deposited on substrates was mentioned in two papers found in the literature[11] [12], though neither examined the adsorption of the bromobenzene molecules to the catalyst. It appears therefore that adsorption of the molecule to gold and silver nanoparticles, a first step in the catalytic process under discussion, is an under-studied phenomenon and a greater understanding would be beneficial. X-ray photoelectron spectroscopy has been performed on pure metal clusters and clusters with bromobenzene adsorbed to the surface. The fact and details of the adsorption have been possible to establish via spectral analysis of $Au\ 4f$, $Ag\ 3d$, $Br\ 3d$ and $C\ 1s$ photoelectron spectra.

1.3 Motivation for Tin and Tin Oxide Studies

Tin oxides have become a topic of intense study in nanoscience, with applications in gas sensors[13] [14] & transparent wide gap semiconductors[15]. There are two stable forms, namely tin (II) oxide (SnO) and tin (IV) oxide (SnO_2), which have very different electronic structures and which are often present together in samples[1]. The significant differences should be a ready means of identification via x-ray photoelectron spectroscopy

(PES), known to be a sensitive tool for determining oxide states, however this has not been so clearly achieved.

The so-called chemical shifts between tin oxides (relative to metallic tin), of the $4d$ core level spectra of tin, within the oxide mixture have been previously obtained from samples where the closely located spectral peaks have not been possible to resolve[1]. The same paper finds the electron binding energy separation between metallic tin and SnO_2 to be approximately 2.0 eV. It is worth noting therefore that this deviates significantly from the similar germanium $3d$ core level, where the separation between the metallic state and germanium (IV) oxide (GeO_2) is approximately 4 eV. Together these issues evoke the question of whether measurements regarding the binding energy shift for SnO_2 are correct. This question has been discussed in literature for many years and has been addressed in several works. The discussion was summarised in, for example, studies by Padova et al[1]. The discrepancy in different results however has not been clearly explained. A possible source of error is the absolute binding energy calibration. In surface science, measurements on semiconductors such as these oxides can often only be taken with respect to the bottom of the bandgap: as opposed to the Fermi edge in metals. Since tin (II) oxide and tin (IV) oxide have significantly different bandgaps this can lead to discrepancies.

Work at MAX-lab has sought to clarify this issue by generating a beam of free nanoparticles/clusters and controlling the oxygen environment in the process of tin oxide formation. As mentioned above free nanoparticles are advantageous model systems to study chemical properties undisturbed by the substrate and measurements may be taken relative to the so-called vacuum level to establish a truly absolute binding energy scale. The photoelectron signal of the clusters can be monitored to determine at under which conditions a pure SnO or SnO_2 response may be measured.

2 Theory

2.1 X-ray Photoelectron Spectroscopy

X-ray photoelectron spectroscopy (XPS) is a technique based on the photoelectric effect and was developed, amongst others, by Kai Siegbahn of the University of Uppsala in the 1960's[16]. It works by irradiating the sample with a monochromatic source of soft x-rays which causes the photoemission of electrons from the core levels. Figure 2 illustrates a core-level photoemission process using the electron energy scheme typical for the metals of the 2nd row of the periodic table. For these metals the electronic levels with the principle quantum number $n = 1, 2$ are the fully filled core-levels and the electrons with $n = 3$ form the valence band. The highest occupied level of the valence band is marked as E_f in the figure. For metallic clusters the situation is similar. Valence levels may be explored using ultraviolet light in place of x-rays. The kinetic energy of these electrons is then related to their binding energies, which can be used to identify the elements comprising a sample and their chemical environment.

$$C + h\nu \quad \rightarrow \quad C^{+} + e^{-} \tag{3}$$

Equation 3 describes how for a free neutral cluster, C, a constituent atom may absorb an irradiating photon. If this photon has energy greater than that which binds an electron, $e-$, the latter will be ejected and the cluster is left in a positively charged state, $C+$. If the absorbing atom is not from the surface layer the ejected electron will have to travel through the upper layers before it is detected.

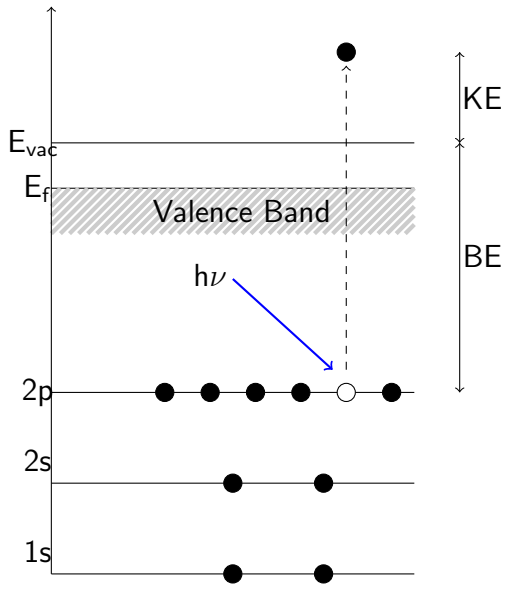

Figure 2: Schematic representation of the core-level photoemission process using the energy scheme typical for the metals of the 2nd row of the periodic table. For these metals the electronic levels with the principle quantum number $n = 1, 2$ are the fully filled core-levels and the electrons with $n = 3$ form the valence band. The highest occupied level of the valence band is marked as E_f in the figure. For metallic clusters the situation is similar.

The probability that an initial state electron will undergo an excitation into a free continuum state is represented by the so-called ionisation cross-section. This is energy

dependent and subsequently the excitation energy can be selected to match the ionisation probability maximum according to the electron energy level to be targeted.

The limiting factor to how far an electron may travel through a "bulky" sample, or a cluster, is determined by its inelastic mean free path: which is the average distance an electron may cover before encountering its first inelastic scattering event[17]. This distance is dependent upon the electrons kinetic energy and has not been shown to be strongly material dependent[18], hence a so-called universal curve amongst the elements is shown in figure 3. The curve illustrates the mean free path dependence on kinetic energies for various materials.

Considering the diagram in figure 3 it is evident that photoelectron spectroscopy is largely a surface sensitive technique which only explores the first few nanometres below the surface of a sample, as only electrons in this region may escape without energy loss. Those electrons which do undergo significant inelastic collisions contribute to the background of the spectrum towards higher binding energies.

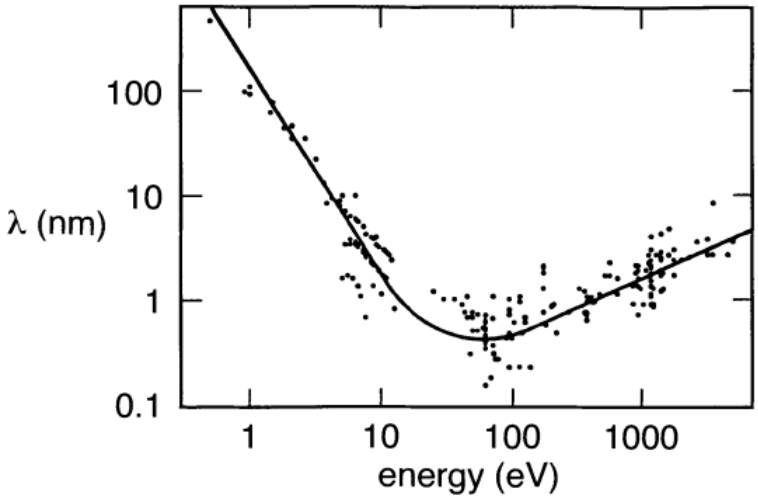

Figure 3: Taken from Lüth[19]. Compiled inelastic mean free path for various materials using data from Seah & Dench[20]. The line indicates the "Universal Curve".

The angle at which the radiation impacts the target also has an effect on the surface sensitivity of the technique. For planar samples a shallow angle of incidence, defined as the angle between the normal to the surface and the radiation direction, makes the technique more surface sensitive, while an angle of 90° would maximise the signal from the sample's inner part. For free clusters studied in the present work however, this will not have an affect as their curved surface and random orientation in the beam results in an even distribution of incidence angles.

Once the electron escapes into the vacuum it is collected and analysed by the detector mechanism, which relates the electron's kinetic energy to the photon energy and to the binding energy of said electron. The relation used is given by equation 4.

$$E_{kinetic} = h\nu - (E_{final} - E_{initial}) = h\nu - E_{bin} \tag{4}$$

The electron signal intensity is plotted versus the binding energy to establish a spectrum. The features of this spectrum can be interpreted to gain insights into the cluster, such as: the binding energy of the electrons, the size of the cluster (via the aforementioned LDM theory, the cluster's chemical composition and the proportion of each element/molecule within the cluster (estimated via the relative intensity of their respective peaks).

2.2 Light Source

2.2.1 Synchrotrons

The light source employed is a third generation synchrotron, namely the MAX-II storage ring at the MAX-lab light source facility in Lund, Sweden.

A synchrotron is an evacuated ring containing circulating electrons. This circular motion is enforced using bending magnets positioned between straight sections. The general layout of a synchrotron may be seen in figure 4. The circulating electrons emit electromagnetic radiation across a broad range of frequencies. Use of a synchrotron is preferable to other X-ray sources due to the its high flux and the possibility to tune the frequency of the radiation.

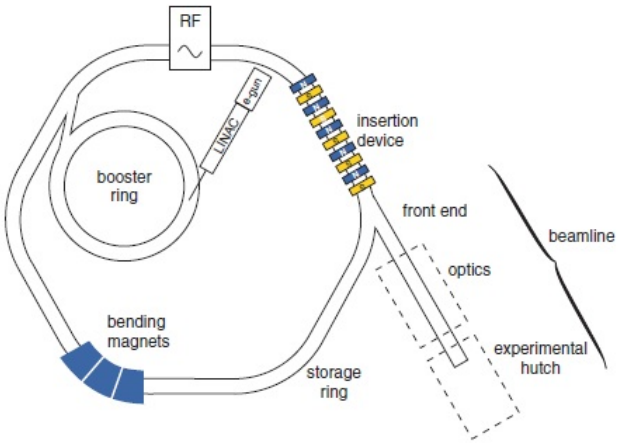

Figure 4: Taken from Willmott[21], Chapter 3. A simplified schematic of a third generation synchrotron, detailing bending magnets, insertion devices, beamlines and the radio frequency (RF) cavity restoring energy to depleted electrons. Also shown is a booster ring to add energy to injected electrons prior to entering the storage ring. MAX-II does not employ such a device.

2.2.2 Synchrotron Radiation

An accelerated charged particle loses energy in the form of electromagnetic radiation, emitted perpendicular to the vector of acceleration. If accelerated along the axis of its motion this radiation will be emitted perpendicular to its path, while if the particle follows a curved trajectory the radiation is emitted tangential to its arc of motion, i.e. in line with its instantaneous velocity.

$$\frac{\partial P(t')}{\partial \Omega} = \frac{e^2}{4 \cdot \pi \cdot c} \frac{|\mathbf{n} \times \{(\mathbf{n} - \boldsymbol{\beta}) \times \dot{\boldsymbol{\beta}}\}|^2}{(1 - \mathbf{n} \cdot \boldsymbol{\beta})^5} \tag{5}$$

The radiation pattern is described by the relativistic form of the Larmor formula, which expresses the power radiated per unit solid angle[22]. The generalised form of this formula is equation (5). The pattern is shown in figures 5a & 5b for a particle moving at non-relativistic velocities. In this equation $\boldsymbol{\beta}$ and $\dot{\boldsymbol{\beta}}$ denote $\boldsymbol{v}/c$ and $\dot{\boldsymbol{v}}/c$ respectively, where $\boldsymbol{v}$ is the velocity of the particle and $\dot{\boldsymbol{v}}$ is its acceleration. γ is the Lorentz factor. The vector $\mathbf{n}$ is a unit vector describing direction. For a more detailed description the reader is referred to the book by Jackson[22]. A synchrotron's benefits become apparent when

examining relativistic electrons such as in figure 6a & 6b. In these cases the radiation pattern is skewed in the direction of the particles motion. Figure 6b illustrates the form taken by synchrotron radiation. In this case, as velocity increases the rear lobe flattens, folds back on itself and eventually, at highly relativistic velocities, overlaps with the forward lobe. This leads to an intense and tightly focused beam of radiation.

$$\frac{\partial P(t')}{\partial \Omega} = \frac{e^2 \cdot \dot{v^2}}{4 \cdot \pi \cdot c^3} \frac{sin^2\theta}{(1-\beta)^5} \tag{6}$$

$$\frac{\partial P(t')}{\partial \Omega} = \frac{e^2}{4 \cdot \pi \cdot c^3} \frac{|\dot{\boldsymbol{v}}|^2}{(1-\beta \cdot cos\theta)^3} \left[1 - \frac{sin^2\theta \; cos^2\phi}{\gamma^2(1-\beta cos\theta)^2}\right] \tag{7}$$

Equations 6 & 7 are the specific forms of the Larmor Formula for these two cases: where the symbols v and $\dot{\boldsymbol{v}}$ stand for the velocity and acceleration respectively. Equation 6 describes parallel acceleration and 7 describes perpendicular acceleration.

Modern *third generation* synchrotrons distinguish themselves from previous generations using *insertion devices* to further enhance the intensity of the beam[21]. Insertion devices such as *undulators* and *wigglers* force the electrons to follow a wavelike or "undulating" motion via a periodic array of magnets. This motion causes electrons to emit a pulse of radiation via the aforementioned process with every crest and trough of their oscillation. This causes the radiation to have a greater flux than could be provided by electrons accelerated bending magnets.

In the case of undulators the radiation emitted at each electron's instantaneous position overlaps and certain wavelengths interfere constructively, producing a spectrum consisting of a fundamental frequency in addition to higher harmonics.

$$\lambda_l = \frac{\lambda_u}{2\gamma^2}(1 + \frac{K^2}{2}), \qquad K = \frac{eB_0}{mck_u} \tag{8}$$

Equation 8 describes the fundamental frequency of the undulator where, λ_l is the emitted wavelength, λ_u is the periodicity of the magnetic arrays, γ is the Lorentz factor, K is the deflection parameter, B_0 is the maximum magnetic field between the arrays and $k_u = 2\pi/\lambda_u$. Manipulating the separation between magnet arrays changes B_0, shifting the peaks to desired wavelengths.

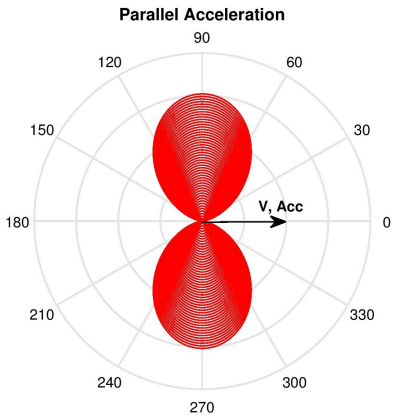

(a) Non-relativistic electron with parallel acceleration.

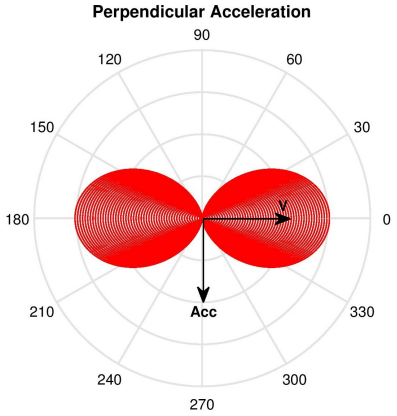

(b) Non-relativistic electron with perpendicular acceleration.

Figure 5: The power radiated per unit solid angle for non-relativistic electrons.

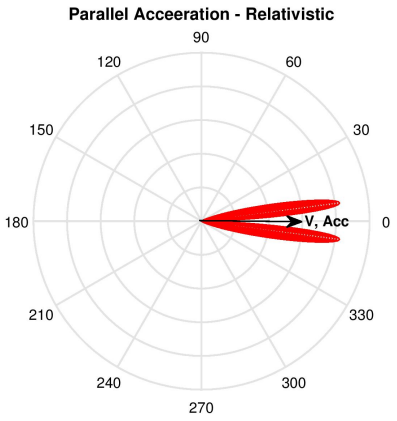

(a) Relativistic electron with parallel acceleration.

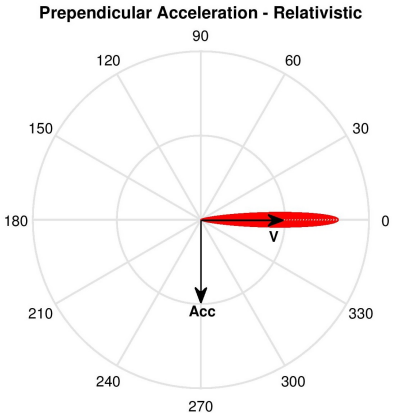

(b) Relativistic electron with perpendicular acceleration.

Figure 6: The power radiated per unit solid angle for highly relativistic electrons with velocity of $2.9 \cdot 10^8\ ms^{-1}$. Figure **b** illustrates the form the radiation field takes for relativistic particles undergoing acceleration perpendicular to their motion, i.e. Synchroctron radiation.

3 Equipment

3.1 Beamline I411

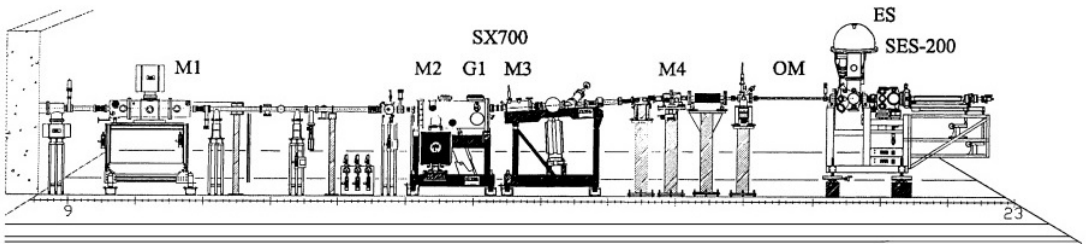

Figure 7: Layout of the I411 beamline taken from Bassler[23]. The Scienta 200 analyser (SES-200), has been replaced by a Scienta R4000.

I411 beamline employs an undulator as described in section 2.2.2, producing radiation in the 40 - 1500 eV range. This radiation is focused by a a spherical mirror (M1) onto the first mirror (M2) of the monochromator arrangement. The monochromator is a modified Zeiss SX700 model consisting of a plane mirror (M2), plane diffraction grating (G1) with 1221 lines/mm and a plane elliptical focusing mirror (M3)[24]. The plane mirror and grating are rotated in unison to scan across the photon energies, while M3 is fixed, with an exit arm length of 1.5m focusing the monochromated light onto the exit slit 17146mm from the undulator.

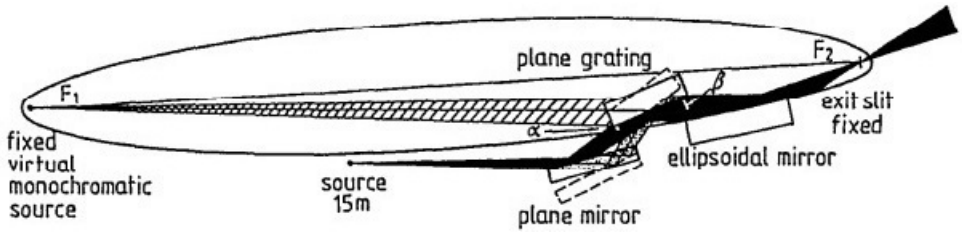

Figure 8: Taken from Domke[24]. A fixed virtual source is focused onto the exit slit. A fixed source avoids defocusing effects of the grating. The lack of an entrance slit is due to its design for low emittance sources.

The light which passes through the exit slit then undergoes both meridional and sagittal focusing, via a toroidal mirror (M4), to a focal point within the end station's experimental chamber where the sample is held. This chamber is designed for experiments with gaseous samples, so that the vacuum within it can be far from the so-called UHV (ultra-high vacuum) conditions: in the $10^{-6} - 10^{-5}$ mbar range. Since the rest of the beamline must be maintained at an ultra-high vacuum of $10^{9} - 10^{10}$ $mbar$ in order to prevent x-ray radiation losses and contamination in the ring, a differential pumping stage is required after the M4. Between this pumping stage and the end station is situated a one meter section which is free for users to place additional equipment as required.

3.2 Detector

The Scienta R4000 is a hemispherical-design electron energy analyser utilising an electrostatic lens and two concentric, charged, hemispheres of opposite polarity as illustrated in figure 9. A potential difference between the hemispheres forces electrons into a curved

trajectory and disperses them as a function of their kinetic energy. For an established potential difference only electrons of a well-defined kinetic energy will traverse the hemispheres and strike the detector. This energy is referred to as the pass energy, E_p. This pass energy together with the spherical electrode radius R and the spectrometer entrance slit S define the kinetic energy interval ΔE projected onto the detector.

$$\Delta E = E_p \cdot \frac{S}{2 \cdot R_o} \tag{9}$$

The detector consists of multiple channels, each of which may have a slightly different detection efficiency[25]. To overcome this problem the detector is operated in the so-called swept, or dithering, mode for the experiments in this thesis. In this mode the electrostatic lens both focuses the photoelectrons onto the entrance and retards/accelerates them as desired to maintain a constant pass energy while scanning across kinetic energies. The dispersed electrons are swept across the micro-channel plate (a part of the detector), so that all energies in the resulting spectrum are detected by each channel for an equal amount of time. However, at low pass energies the electron transmission is reduced as low energy electrons fail to pass through the lens. Should the count rate be insufficient however, increasing the pass energy would have the effect of increasing electron transmission at the sacrifice of resolution.

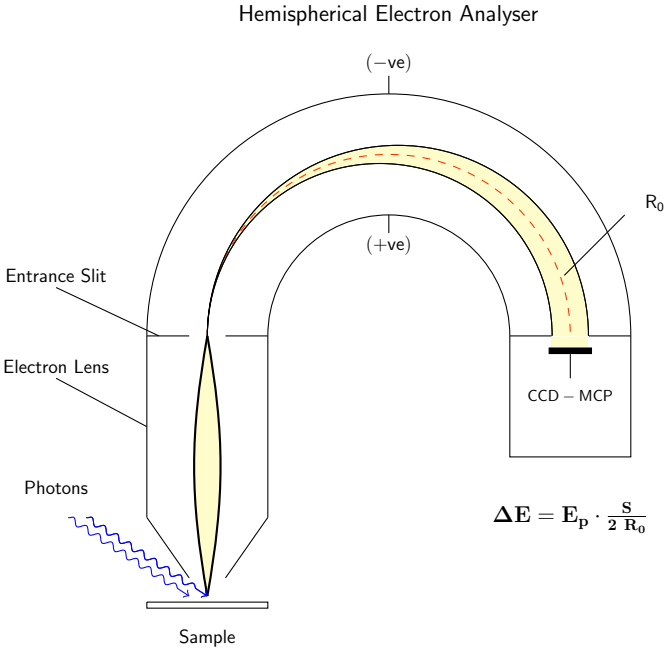

Figure 9: The electron analyser. Yellow indicates the presence of electrons. The red trace indicates the path travelled by an electron at exactly the pass energy.

3.3 Magnetron Sputtering-based Cluster Source

To create the metal clusters it is necessary to first produce a primarily metal vapour out of the metal of interest, before causing the vapour to condense into clusters. There are several possible methods to produce this vapour[26] such as thermally using a resistive oven, through laser ablation or by sputtering processes, such as the one used to produce vapours in the experiments reported on in this thesis.

Sputtering is defined as the removal of surface atoms due to energetic particle bombardment[27]. Materials to be evaporated are attached to a magnetron in a solid form called a target. The magnetron in the present cluster production method is placed inside an aluminium metal cylinder with two gas injection lines, one for argon and one for helium. The magnetron is mounted in a liquid nitrogen cooled cryostat, within an evacuated chamber. The cryostat is then filled with a process gas (Ar), which flows through it continuously.

A negative electrical potential is applied to the magnetron (cathode) of several hundred volts. This potential will cause ever present free electrons to accelerate away from the magnetron. When these electrons collide with an argon atom they strip it of an electron, ionising the atom and creating a plasma. The magnetron in operation may be seen in figure 10**a**. This potential and the plasma discharge are why the magnetron is placed within a vacuum. This discharge can only be ignited at very low pressures and the gas must be in a rarefied condition. Also in the air the surface of the target would quickly develop and insulating oxide layer, halting the discharge, since the electrical potential can only be sustained if the target is conductive.

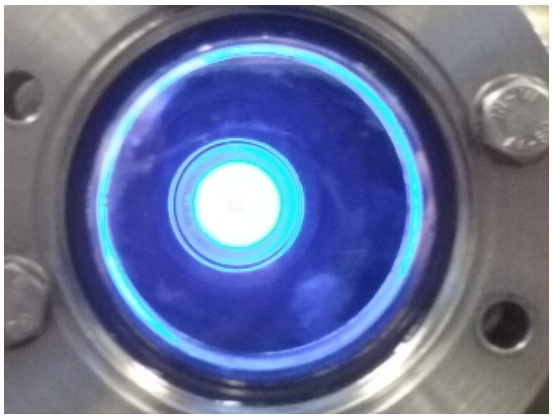

(a) Magnetron sputtering source in action.

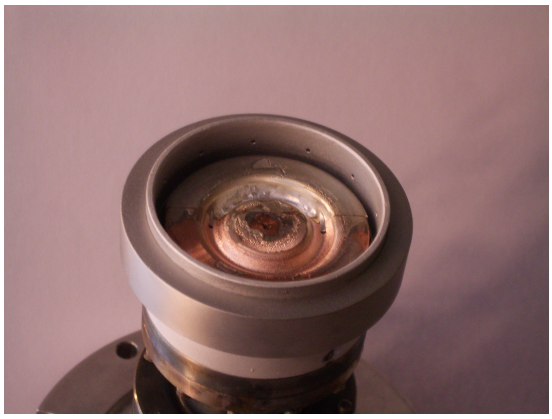

(b) Magnetron with 2 inch diameter silver target.

Figure 10: Images of the magnetron during and after use. The blue plasma in figure **a** is the result of electron transitions in the argon. In figure **b** the erosion due to the circular path of the electrons is evident and above the target, on the inside of the magnetron, the gas injection holes may be seen.

The free electrons are confined to an area close to the target by magnets, which leads to a greater plasma density and subsequently higher sputtering rates[28]. The magnets cause the electrons to move in a circular arc increasing the rate of collisions between electrons and the sputtering gas. This increases the probability the electrons will ionise a neutral argon atom[29]. The erosion on the target caused by this path may be seen in figure 10**b**. The positive argon ions are accelerated towards the magnetron and carry enough energy to knock off some of the magnetron's target material. The positively charged ions will then recombine with free electrons to create a neutral atom again.

Aggregation of the produced metal vapour is achieved within the liquid nitrogen cooled cryostat, which consists of a double walled cylindrical chamber (figure 11) with a truncated cone at one end mounted on an XYZ manipulator. The argon and helium gases are cooled through contact with the cryostat walls. These cold atoms then proceed to collide with the sputtered target material atoms thermalising them and causing them to aggregate into clusters. At the end of the cryostat is a copper nozzle which has a long narrow

channel. The primary function of the nozzle is to reduce the exit hole of the cryostat, defining the gas flow rate, extending the condensation time in the cryostat and encouraging aggregation. The nozzle also serves to collimate the beam.

Figure 11: The liquid nitrogen cooled cryostat. The copper end-piece to the left is the nozzle.

The evacuated chamber, referred to as the cluster source, which the cryostat resides in, is attached to another evacuated chamber (ionisation chamber). The gas density inside the cryostat, of a few Torrs, is much greater than in the cluster course. This causes a flow of argon and helium gases which ferries the clusters from the cryostat, through the cluster source, into the ionisation chamber. The only connection between the two evacuated chambers is through a cone shaped copper skimmer with a 2 mm orifice. Although the separation between the cryostat and the ionisation chamber is only several centimetres, the beam will diverge over this distance. The skimmer serves to separate the cluster rich central part of the beam from the divergent parts and from the excessive argon and helium gases.

4 Spectral Response

When the detector scans across a range of energies corresponding to some core-level ionisation and the intensity is plotted against the binding energy, the result is, as a rule, a spectrum consisting of discrete peaks broadened and influenced by various factors.

In the simplest of cases these peaks would be symmetric with no broadening beyond the natural linewidth of the transition. In reality each peak is broadened, reshaped and with their relative intensities influenced in several ways due to peculiarities of the experiment and equipment involved.

4.1 Intensity

The intensity of a peak is to a large extent dependent upon the probability of ionisation (cross-section) at the probing photon's wavelength for the electron involved, the pass energy of the detector, and the angle at which electrons are collected with regard to the ionising radiation.

4.1.1 Cross-Section

As mentioned above the photoionisation cross-section is dependent upon the photon energy. Selecting the optimum wavelength will contribute greatly to the intensity of the spectrum. In fig 12 the photoionisation cross-section for the valence and outer core levels of gold are plotted. From this it can be seen that if the cross-section is considered the only contributing factor, a photon energy which favours ionisation of one electron level will prejudice another. A spectrum will, therefore, inherently portray a warped representation of the system's core-levels and valence levels, making a direct comparison between the relative intensities of peaks a more convoluted endeavour than at first inspection.

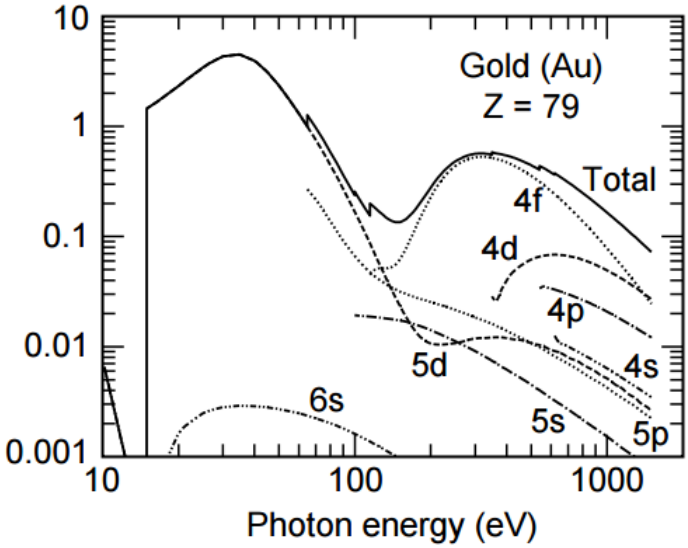

Figure 12: Various core & valence subshell photoionisation cross-sections for gold. The graph may be found in the Center for X-Ray Optics and Advanced Light Source, X-Ray Data Booklet or in .pdf form at xdb.lbl.gov.

4.1.2 Angular Distribution

The energy dependent angular anisotropy parameter ($\beta_{nl}(h\nu)$) for an electron's energy state also contributes to the detected spectral intensity because photoelectrons are not emitted equally in all directions. The intensity of peaks in a spectrum depends therefore upon the angle, with respect to the ionising radiation's electric vector, at which the detector is situated (γ). The analyser in these experiments was positioned at an angle of 90° to this vector. The radiation at the I411 beamline has been polarised in the horizontal plane.

$$\frac{\delta\sigma_{nl}(h\nu)}{\delta\Omega} = \frac{\sigma_{nl}(h\nu)}{4\pi}[1 + \beta_{nl}(h\nu)\frac{1}{2}(3cos^2\gamma - 1)] \tag{10}$$

Equation 10 describes the probability an electron will be ionised and emitted at a specific angleand is given, for example, by Yeh and Lindau[30]. At 90° s orbitals would reduce this equation to zero. In practice however, while the intensity of the s orbital peaks would be greatly diminished they may still be detectable at certain photon energies.

In this equation $\sigma_{nl}(h\nu)$ is the energy dependent photoionisation cross section. Values for the angular anisotropy parameter may be found in various sources, notably the paper by Yeh and Lindau, where the radiation is assumed to be linearly polarised. In their paper the calculations are based on Hartree-Fock-Slater wavefunctions yielding a $\beta_{nl}(h\nu)$ of 2 for s-subshells and from -1 to 2 for others.

4.2 Broadening

A peak in a core-level spectrum may be broadened by a number of different factors. When an atom undergoes core-level photoionisation it will be left in an excited state, which decays with a certain time constant denoted as the lifetime. Subsequently there must exist for all peaks a natural linewidth resulting from the lifetime of the state. The resulting spectral profile has a Lorentzian lineshape. The width of each peak in energy (ΔE) is related to the uncertainty in the lifetime (Δt) of the state by the Heisenberg uncertainty principle, equation 11. The shorter the lifetime of the state, the greater the uncertainty in its energy. This natural linewidth will be to a certain extent obscured due to the limitations of the equipment involved.

$$\Delta E \cdot \Delta t \approx \hbar \tag{11}$$

The spectral profile of Lorentzian lineshape undergoes Gaussian broadening due to the limited monochromaticity of the exciting radiation, the resolution of the detector and thermal broadening. The limitation of the monochromator is primarily due to a combination of the grating's ability to separate wavelengths and the slit widths of the instrument. The electron energy analyser resolution (ΔE_A) is defined by the pass energy and slit width as detailed in section 3.2. The thermal broadening (Δ_{th}) results from the non-zero thermal energy possessed by the sample. The total contribution of these Gaussian broadening sources may be estimated using the following equation.

$$\Delta E = (\Delta E^2_{mono} + \Delta E^2_A + \Delta E^2_{th})^{1/2} \tag{12}$$

4.3 Spectral Features

4.3.1 Lineshape for the Core-Level Ionisation

The different sources of broadening lead to a convolution of Lorentzian and Gaussian lineshapes resulting in a so-called Voigt Profile. In macroscopic solid substances and in nanoscale clusters this profile is then affected by other processes. An ejected photoelectron may lose energy by interacting with other electrons within the sample, exciting them from the valence band to the conduction band. The energy the original electron loses in this process causes it to be registered by the detector at a lower kinetic energy than would otherwise be the case. The probability that the photoelectron will excite another electron to a level within the conduction band decreases as the amount of energy required to do so increases. The result of this is that in metallic solids, where there is no gap between the valence and conduction bands, the spectral peaks possess an asymmetric tail towards higher binding energies. This spectral shape is called a Doniach-Sunjic profile (figure 13 & equation 13). This is then convolved with the Gaussian broadening from the factors described above to form the final broadened lineshape.

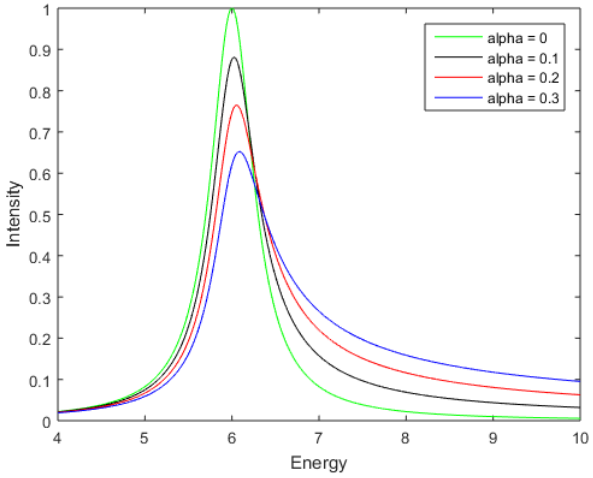

Figure 13: The Doniach-Sunjic profile. The asymmetry parameter (α) determines the emergence of the tail at higher binding energies. When this parameter is set to zero the Doniach-Sunjic profile becomes the simple Lorentzian lineshape.

$$DS(E) = \beta \cdot \frac{cos\left[\pi\frac{\alpha}{2} + (1-\alpha)arctan[\frac{E-E_0}{\beta}]\right]}{[(E-E_0)^2+\beta^2]^{\frac{1-\alpha}{2}}} \tag{13}$$

In equation 13 E is the energy on the binding energy scale; E_0 the peak position; β, half width at half maximum and α, the asymmetry parameter. When α is reduced to 0 the Doniach-Sunjic equation will reduce to that of the original Lorentzian.

For free atoms, where no bands exist, the valence electron can be excited by the outgoing photoelectron to one of several discrete unoccupied energy levels. This results in separate, lower intensity, peaks appearing on the higher binding energy side rather than an asymmetric tail. These peaks are referred to as satellite peaks. In insulators the outgoing photoelectrons can excite valence band electrons over the band-gap into an arbitrary state in the valence band. This leads to the presence of an additional band in the core-level spectra of dielectrics, the band separated from the parent core line by the energy equal to the band gap value.

4.3.2 Doublets

Energy levels are described by the nl_j nomenclature, where n is the principle quantum number, l is the orbital angular momentum quantum number and j is the total angular momentum quantum number. The total angular momentum is calculated as $j = l \pm s$ where s is the total spin of all electrons.

A phenomenon called Spin-Orbit coupling causes the peaks in many cases, including in the present work, to be split into doublets for all $l > 0$. The ratio of the areas under these doublet peaks will be dependent upon the degeneracy of each state (table 1), where the degeneracy is calculated as $2j + 1$. The peaks representing a higher value of j have a lower binding energy and a greater degeneracy, which subsequently means they form the more intense of the doublet peaks.

Table 1: Spin-Orbit Splitting

Subshell	j Value	Degeneracy (2j +1)	Ratio
s	1/2	2	N/A
p	3/2, 1/2	4, 2	2:1
d	5/2, 3/2	6, 4	3:2
f	7/2, 5/2	8, 6	4:3

4.3.3 Chemical Shifts

While each element posesses a unique 'fingerprint' of core-level binding energies, variations can be detected due to different chemical environments of the same element. In the initial state the total energy of the system is influenced by the bonding between atoms, while for the final state variations occur due to the actions of neighbouring atoms which increase or decrease the electrostatic potentials at the position of an ionised atom[31]. This results in a shift in the binding energy, which is defined as a difference between the initial and the final total energy of the system. This is referred to as a 'chemical shift'.

5 Treating the Data

The raw data from the detector was provided in .pxt format and processed using the commercial software Igor Pro 6.37 with the addition of the package developed by E.Kukk[32]. This software can perform various forms of arithmetic and fits model spectral peaks to the experimental data through least-squares fit methods. The specific parameters of the fit: asymmetry, position, intensity ratios and Lorentzian and Gaussian peak widths, can be specified by the user if such parameters are known. The goodness of the fit is given by the parameter χ^2, a measure of the difference between the data and the fitted line. Ideally this should be near zero.

The peak profile may be set as a Voight, Fano, Doniach-Sunjic or user defined profile. These peaks may be linked in terms of any of their parameters to achieve a more physically realistic fit. In this work a Doniach-Sunjic profile was used for metallic clusters and a Voight profile for non-metallic substances.

For the free clusters, spectra were calibrated using the well understood argon $3p$ or $2p$ peaks present in the spectra as a result of the magnetron operating.

6 Results & Analysis

6.1 Gold Clusters, Silver Clusters and Bromobenzene

6.1.1 Gold Clusters, Silver Clusters and Unadsorbed Bromobenzene Vapour

To investigate the adsorption of bromobenzene on silver and gold clusters, spectra were taken of the specific electron energy levels, namely: the silver $3d$ level, gold $4f$ level, bromine $3d$ level and silver $3d$ level. Bromobenzene, gold and silver were all initially examined in their isolated forms. For comparison these same levels were then investigated after the clusters were exposed to the bromobenzene vapour.

Using reference data from the X-ray Data Booklet it is taken that the peaks for the silver $3d$ level are located at 374.0 eV and 368.3 eV with respect to the Fermi level. Since all data from the experiments relevant to this thesis are taken with respect to the vacuum level it is necessary to add the workfunction to these reference values.

The workfunction for silver shows a distinct dependence on which crystal plane the electron is escaping from, though a value of 4.26 eV is often quoted for a polycrystalline form[33] [34] and is the value used in this thesis. This yields reference peaks with respect to the vacuum level of 378.26 eV and 372.56 eV. The spectra for the silver $3d$ level were calibrated using the argon $2p_{3/2}$ ionisation energy for free atoms located at 248.63 eV[35]. After calibration the data shows peaks, illustrated in figure 14, at 378.383 eV ($3d_{3/2}$)and 372.379 eV($3d_{5/2}$). This is a shift of +0.18 eV for the silver $3d_{5/2}$ peak and of +0.12 eV for the $3d_{3/2}$ peak, from what would be expected in the bulk material. The separation between the fitted doublet peaks does not match that of the reference data by 0.3 eV. This separation was left free during fitting as the separation quoted by the reference source clearly did not adequately fit the experimental data.

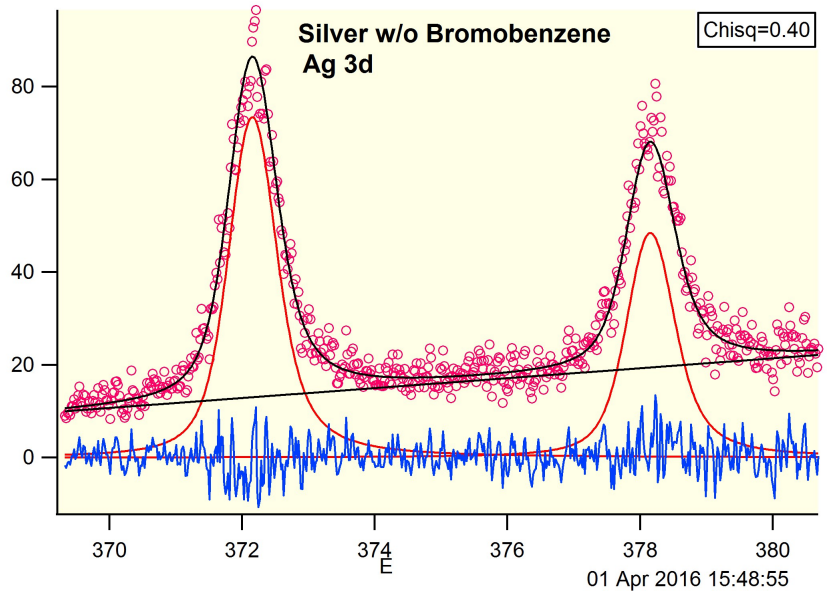

Figure 14: Silver $3d$ spectrum without bromobenzene. The red hollow circles are the experimental data. The blue line indicates the difference between the fitted line and the experimental data. The red curves are the fitting peaks while the black curve is the sum total of these model peaks at each energy step. The straight black line is the background. Calibration was performed using the Ar $2p$ level.

The workfunction of polycrystalline gold is often quoted as 5.1 $eV \pm$ 0.1 eV [33] [34], though recent work has found it to be 5.2 eV [36]. In this thesis the value of 5.2 eV was used. Reference data taken from the X-ray Data Booklet gives ionisation energies with respect to the Fermi level of 87.6 eV and 84.0 eV for the $4f$ level. With respect to the vacuum level these values become 92.8 eV and 89.2 eV. The spectra were calibrated using scans of the Ar $3p$ spin-orbit split peaks located at 15.7 eV and 15.9 eV according to the X-ray Data Booklet. Gold $4f$ doublet peaks, illustrated in figure 15, were found at 93.164 eV ($4f_{5/2}$)and 89.472 eV ($4f_{7/2}$). This is a shift of +0.272 eV for the gold $4f_{7/2}$ peak and +0.36 eV for the gold $4f_{5/2}$, from the bulk material.

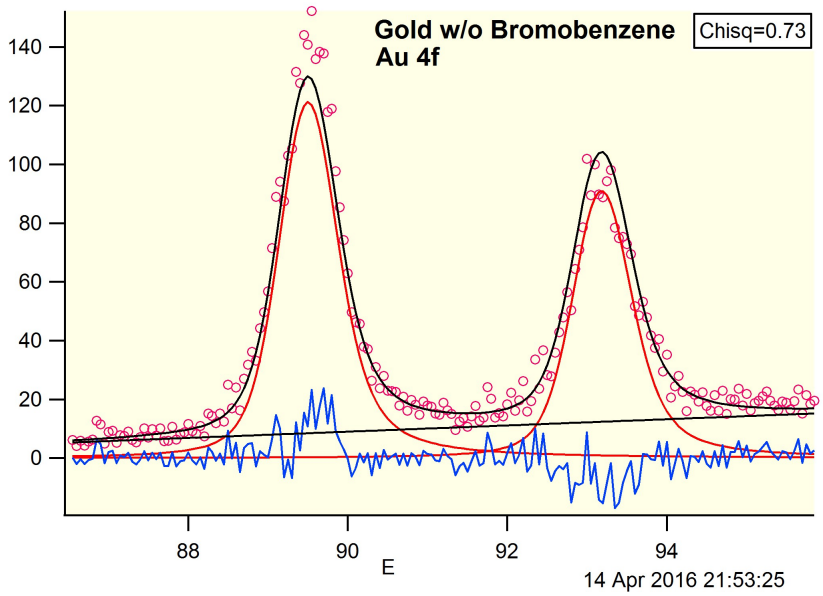

Figure 15: Gold without bromobenzene. Gold 4f level. The $4f_{5/2}$ peak is to the right and the $4f_{7/2}$ peak to the left. Chisq is a measure of the "goodness" of the fitting.

The free bromobenzene vapour molecules were investigated prior to cluster exposure by injecting the vapour and recording spectra in the bromine $3d$ level. Reference values for the bromine $3d$ level taken with respect to the Fermi level are 70 eV and 69 eV. This spectrum was fitted twice. Once when the silver experiments were performed and once when the gold experiments were performed. The results are in good agreement, with 76.349 eV ($4f_{5/2}$) & 77.349 eV ($4f_{3/2}$) provided by the former and 76.335 eV ($3d_{5/2}$) & 77.335 eV ($3d_{3/2}$) provided by the latter. One of these spectra is illustrated in figure 16. For bromobenzene, the exact absolute energy of these peaks is not of the greatest importance as it is the emergence of a shifted component after exposure to the clusters which is of interest, as this would provide evidence of adsorbed molecules.

The shifts in the Au $4f$ and Ag $3d$ doublets from their bulk values may be used to determine the size of the clusters being produced by employing the liquid drop model. This model makes use of the work function of both the clusters and the materials bulk form. It has been observed however, that size dependent shifts in the work function are mirrored by shifts of an equal size in the core levels [37]. Since it is easier to more accurately determine the position of the core levels than of the work function it is preferable to use these peaks for size determination using the same equation given above. In this manner the size of the silver clusters was determined via the shifts in the silver $3d$ level. With the values of 372.379 eV and 378.383 eV quoted above, the approximate size of the silver clusters is found to be between 30-45Å depending on which of the doublet peaks is used.

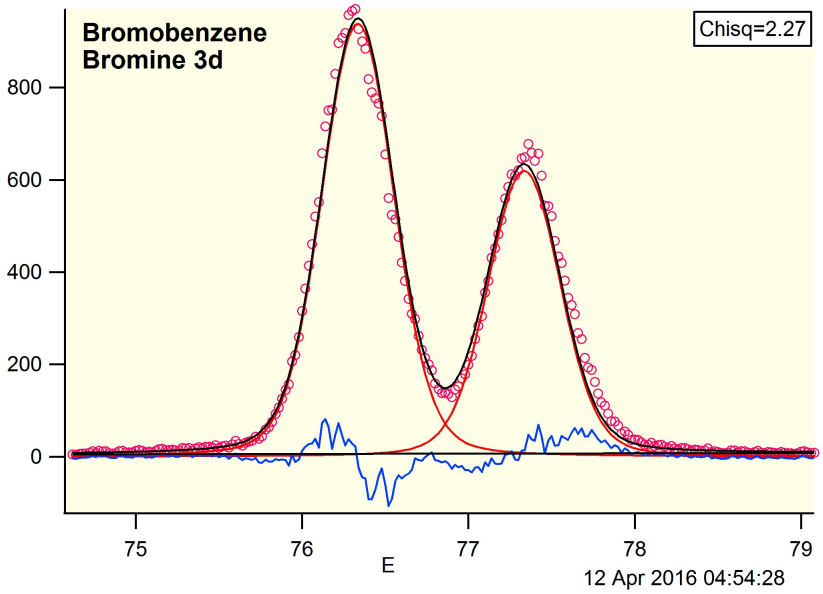

Figure 16: Bromine 3d level of the bromobenzene vapour. Fitted using two Voight profiles for the $Br\ 3d_{5/2}$ (left) and $Br\ 3d_{3/2}$ (right) spin orbit components.

This particular uncertainty is a result of the disharmony between the separation of the fitted results & that of the X-ray Data Booklet reference results. The approximate size of gold clusters is found to be between 15-20Å depending on which of the doublet peaks is used.

Valence spectra were also used to estimate the size of the particles. This method is particularly subjective because there are many ways to estimate the work function from these spectra. In this thesis it was taken as the halfway point down the trailing edge of the valence band. This method resulted in a cluster size of 38.6Å for silver clusters and 17.4Å for gold clusters. Due to the many sources of error present when performing these experiments, it is impossible to give more than a rough estimate of the cluster's size. It should also be noted that these sizes would only reflect the mean size of a broad distribution of sizes formed in the beam.

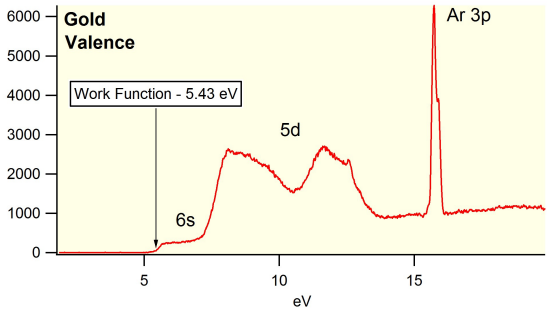

(a) Valence spectrum for gold.

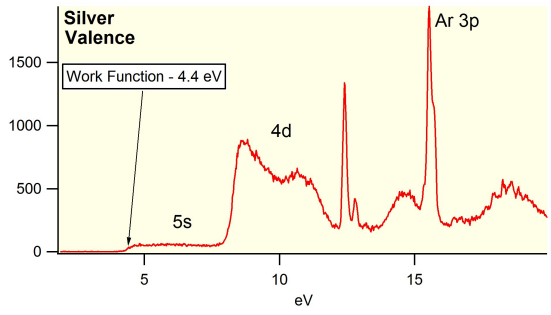

(b) Valence spectrum for silver.

Figure 17: Valence spectra for gold and silver, displaying clear $5d$ & $6s$ bands for gold and $4d$ & $5s$ bands for silver. The intense $Ar\ 3p$ doublet (unresolved) used to calibrate the spectra is present towards the higher binding energy side.

6.1.2 Adsorption of Bromobenzene to Gold Clusters and Silver Clusters

Silver clusters were then exposed to the bromobenzene vapour and spectra of both the bromine $3d$ doublet and silver $3d$ doublet were taken. The silver $3d$ doublet (figure 18**a**) presented at 377.800 eV and 371.824 eV for the $3d_{3/2}$ and $3d_{5/2}$ orbitals respectively. The bromine $3d$ doublet (figure 18**b**) presented in both its original form and a less intense secondary doublet shifted towards lower binding energies. The shifted Br $3d_{5/2}$ and Br $3d_{3/2}$ peaks are located at 75.084 eV and 76.084 eV respectively. This can be taken as evidence that adsorption has indeed taken place as both silver and some of the bromobenzene has undergone a chemical shift, indicating a new chemical environment after exposure.

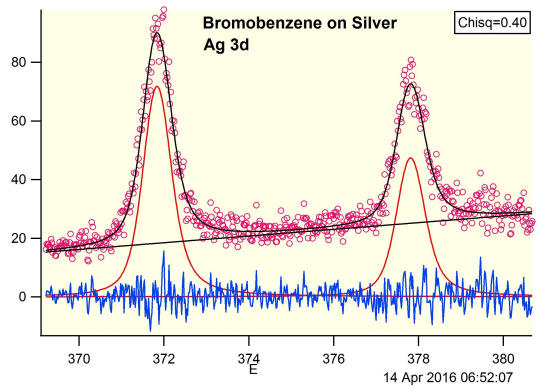

(a) Silver $3d$ region after silver clusters were exposed to bromobenzene vapour.

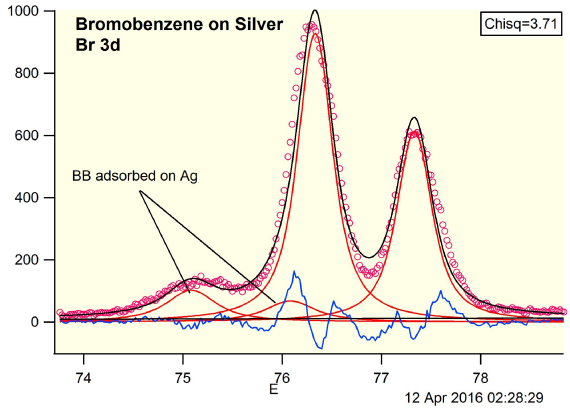

(b) Bromine $3d$ region after silver clusters were exposed to bromobenzene vapour.

Figure 18: The red hollow circles are the experimental data. The blue line indicates the difference between the fitted line and the experimental data. The red curves are the fitting peaks while the black curve is the sum total of these model peaks at each energy step. The straight black line is the background. In figure **b** intense peaks are due to unabsorbed bromobenzene, while weak peaks are the same Br $3d$ peaks shifted to lower energies due to adsorption on silver.

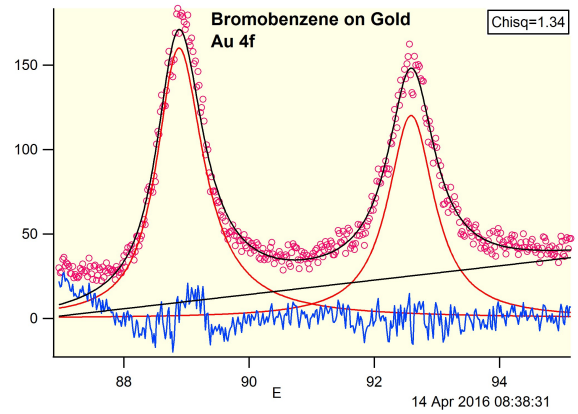

(a) Gold $4f$ region after gold clusters were exposed to bromobenzene vapour.

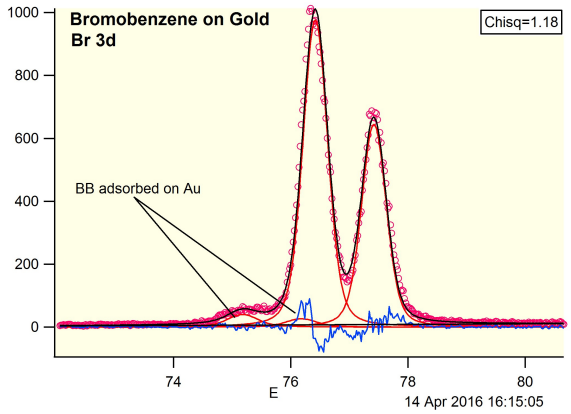

(b) Bromine $3d$ region after gold clusters were exposed to bromobenzene vapour.

Figure 19: In figure**b** intense peaks are due to unabsorbed bromobenzene, while weak peaks are the same Br $3d$ peaks shifted to lower energies due to adsorption on gold.

For the case of the gold clusters, after their exposure to bromobenzene, a broad spectrum was collected. This spectrum was isolated into the two regions regarding the $4f$ level of gold (figure 19**a**) and the $3d$ level of bromine (figure 19**b**). The $4f$ level of gold was found to present in peaks at 88.879 eV and 92.588 eV for the $4f_{7/2}$ and $4f_{5/2}$ orbitals respectively. The $3d$ level of bromine again presented in both its original form and a less intense secondary doublet shifted towards lower binding energies. The bromine $3d_{5/2}$ and $3d_{3/2}$ peaks were found at 76.418 eV and 77.418 eV respectively. The shifted $3d_{5/2}$ and $3d_{3/2}$ peaks are located at 74.179 eV and 75.179 eV respectively.

Spectra were also collected for the carbon $1s$ level for the bromobenzene vapour both before and after adsorption to silver had taken place. These two spectra are illustrated in figures 20**a** and 20**b**. The peaks are low intensity due the electrons being ejected from s orbitals and the detector being positioned at 90° to the radiations electric vector. Two distinct peaks are observable due to the carbon atoms in the bromobenzene phenyl ring occupying four inequivalent positions, which are illustrated in figure 21.

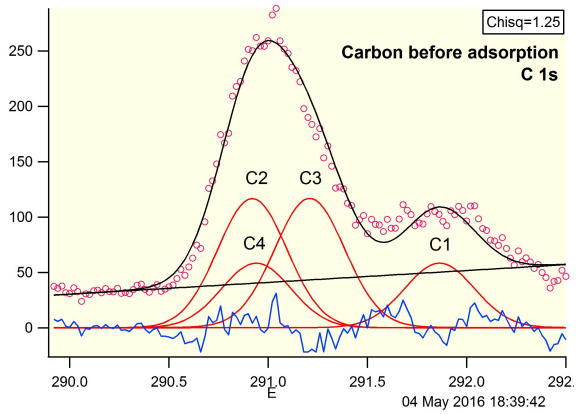

(a) C $1s$ spectrum prior to adsorption.

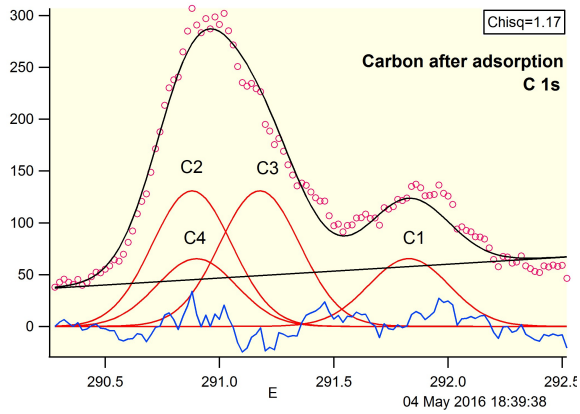

(b) C $1s$ spectrum after adsorption.

Figure 20: The carbon $1s$ spectra were fitted using four peaks with a 1:2:2:1 intensity ratio for the C1, C2, C3 and C4 carbon atoms, in keeping with the paper by Ohta et al[38]. The spectra were calibrated using the nearby argon $2p$ peaks.

The carbon peaks were found to exhibit no change between pre-absorption and post-absorption states greater than the order of 10^{-2} eV: too small to indicate a chemical shift. This lack of a chemical shift suggests bromobenzene does not adsorb via the carbon atoms: only the bromine atom. This is supported by work concerning the adsorption of iodobenzene (another aryl halide) to gold nanoparticles (a similar metal), where XPS and near edge x-ray absorption fine structure (NEXAFS) spectroscopy determined that the molecule adsorbed via the iodine atom at an angle of 15° to the surface of the particles[10].

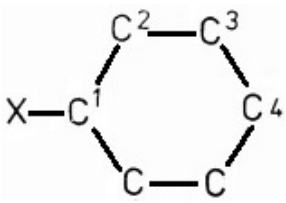

Figure 21: Generic monosubstituted benzene ring, representative of bromobenzene, with the four positions of carbon indicated. Image taken from Ohta et al[38] and modified.

An approximate value for the coverage fraction may also be established when it is noted that photoelectron spectroscopy is a surface sensitive technique. Given the assumption that only the single surface layer of the cluster contributes to the signal, an expression for the intensity of a peak may be developed.

$$I_m \sim n \cdot N_s \cdot P_m \tag{14}$$

Equation 14 is this expression, where I_m is the intensity of the metal peak, n is the number of metal clusters in the ionisation volume, P_m is the probability of ionising a metal atom in the cluster and N_s is the number of metal atoms in the cluster.

By making a similar assumption that the bromobenzene molecules form a single layer on the clusters and that they cover all clusters in the ionisation region, an expression for the intensity of a bromine peak, shifted by adsorption, can be obtained.

$$I_{Br} \sim n \cdot N_s \cdot P_{Br} \cdot Coverage\ Fraction \tag{15}$$

$$\frac{I_m}{I_{Br}} \sim \frac{P_m}{P_{Br} \cdot Coverage\ Fraction} \tag{16}$$

In equation 15 the intensity of the bromine peak shifted due to adsorption is given by I_{Br} and the probability of ionisation for the bromine atoms is P_{Br}. Combining equations 14 and 15 into equation 16 allows the coverage fraction to be estimated.

The probabilities of ionisation for each electron orbital, given the photon energy they were observed at, were taken from tabulated values calculated by Yeh & Lindau[30] and published online[39]. The silver 3d orbital was observed at 448 eV. Using the closest available reference value of 450 eV, P_m $(Ag3d)$ was found to be 4.054 $Mbarn$. The value of P_{BB} was similarly found to be 6.206 $Mbarn$ for 160 eV photons. Following a procedure used in a study of Tin[40], the values of I_m $(Ag3d)$ and P_{BB} were taken as the sum of the area beneath the respective doublet's peaks. This yields 6241 for I_M $(Ag3d)$ & 7505 for P_{BB}. The coverage fraction for bromobenzene adsorbed to silver was subsequently found to be 0.76, i.e, 76% of the surface atoms of the silver clusters are estimated to have an adsorbed bromobenzene molecule. For gold clusters P_m $(Au4f)$ was found to be 1.403 $Mbarns$ for an incident photon of 180 eV. With an I_m of 19019 and I_{BB} of 47723, a coverage fraction of 0.58 was obtained.

These experiments have demonstrated the potential sensitivity of photoelectron spectroscopy to the binding energies of electron energy levels and to the chemical environment of the atoms from which these electrons are ejected. Bromobenzene was found to adhere to both gold and silver clusters via its bromine atom, while the relative intensity of relevant peaks were used to estimate the extent to which the clusters surfaces were coated (76% for silver and 58% for gold). Size-related effects exhibited by metallic clusters on the electron energy levels were exploited to determine the radii of the clusters produced 10-15Å for gold and 30-45Å for silver).

6.2 Tin and Tin Oxides

The tin experiments were conducted on both free and deposited clusters. In the case of clusters containing tin oxide reactive sputtering has been used for their fabrication: oxygen was added to the argon gas feed in progressively higher levels. Spectra of the tin cluster's $4d$ and valence levels were recorded at each oxygen concentration in order to study the oxide state and to determine how best to distinguish the two stable forms of the oxide, tin (II) oxide and tin (IV) oxide from one another and their intermediaries. For free cluster's, spectra were calibrated using the $3p$ level of argon.

In the case of deposited clusters, two composition cases have been studied in the fabrication process: oxygen was added at levels found, for the free clusters, to consist of firstly tin (II) oxide, then tin (IV) oxide. This was confirmed by recording spectra of the clusters prior to deposition upon the silicon substrate. Deposited spectra were then characterised by observing the $4d$ and $3d$ levels of tin, after which they were sent away for characterisation by the scanning electron microscopy (SEM) at the physics department of Lund University. The SEM images were then used to estimate the size of the deposited clusters.

6.2.1 Free Clusters of Tin and Tin Oxide

The $4d$ core-level spectra for the tin clusters, captured at each oxygen concentration, are collected in figure 22. The pure metallic clusters, with no oxygen in the beam, are easily identifiable by a resolvable doublet peak at 28.42 eV $4d_{5/2}$ and 29.47 eV $4d_{3/2}$ in spectrum **a**. This is a shift of 0.1 eV to 0.17 eV from the reference values taken from the X-ray Data Booklet of 23.9 eV and 24.9 eV once the work function has been added. A work function of 4.4 eV was attained as the average of the many different values present in the literature: 4.18 eV[41], 4.3 eV[42] and 4.6 eV[43]. Using the conducting sphere model these results indicate clusters with a radius of $3 - 5$ nm.

At an oxygen concentration of 1.3 % (spectrum **b**) the emergence of another doublet, overlapping strongly with the doublet for metallic tin, is observed. This second doublet has been assigned to the tin (II) oxide and is separated from the metallic tin doublet by 1.3 eV. Padova et al[1] suggested 1.4 eV for the separation between metallic tin and tin (II) oxide. The difference may be due to the method by which the shift is measured. Padova et al measured the shift between the doublets centres of gravity, while for the work in the thesis it is measured as the separation between $4d_{5/2}$ components.

As the relative oxygen concentration in argon (measured in units of partial pressure) increased in the sputtering mixture the oxide response grew and shifted towards higher binding energies. The shift towards higher binding energies has been attributed to the appearance of intermediate oxides with oxidation states between that of tin (II) oxide and tin (IV) oxide. Spectra **c** and **d** in figure 22 exhibit no metallic response and their broad symmetric shape indicates the presence of multiple unresolved peaks. Spectra **c** and **d** are fit well by two doublets, each with the ≈ 1 eV separation exhibited by metallic tin and tin (II) oxide. It should be noted however, that with so many unknowns and the number of possible intermediate oxides states, this cannot be assumed to be a thoroughly unambiguous fit.

At concentrations above the 3 % employed for spectrum **d** the shifts decreased and the peak took on a distinctive asymmetric shape, indicative of a single unresolved doublet. Fitting provides a single doublet of the same separation (≈ 1 eV) observed for the metallic tin and tin (II) oxide. This suggests only one oxide is present in the sample at this

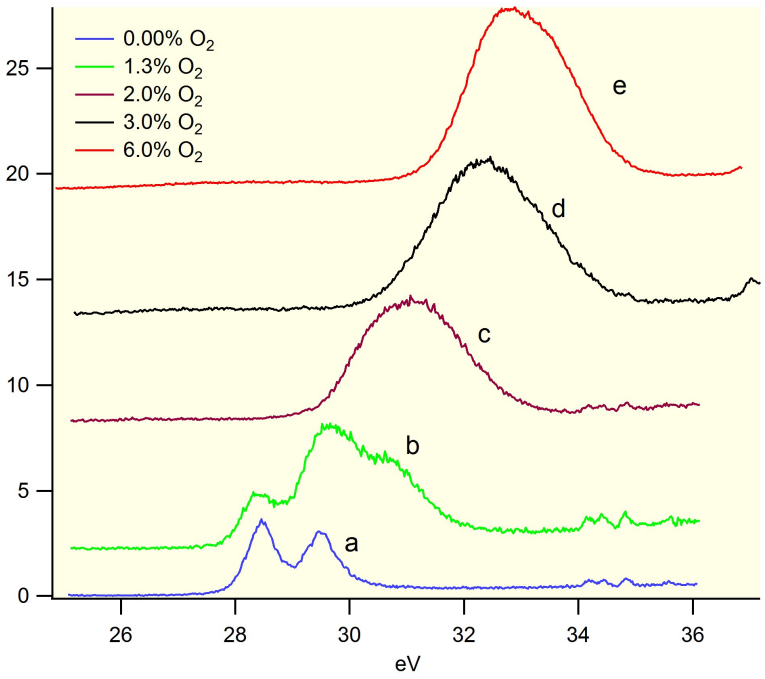

Figure 22: $4d$ core-level spectra of tin clusters forming under various O_2 concentrations, oberved at $h\nu = 60\ eV$. Spectrum **a** is pure tin, **b** is tin & tin (II) oxide and **e** is pure tin (IV) oxide while **c** & **d** are comprised of intermediate oxides.

oxygen concentration and has been assigned to tin (IV) oxide due to its large shift from the metallic state of 4.2 eV. This figure is in keeping with the analogous GeO_2 $3d$ level (4.0 eV). The greatest shift observed by Padova et al[1] in the $4d$ level is 2.0 eV, suggesting the sample used in the previous study was not sufficiently oxidised to establish tin (IV) oxide.

Changes have also been observed in the valence spectra illustrated in figures 23 and 24. Figure 23 focuses on the valence spectra for the lowest oxygen concentrations while 24 shows all valence spectra for comparison.

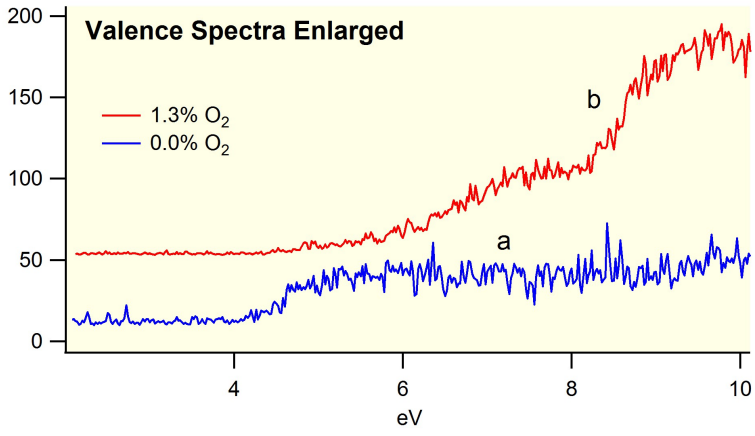

Figure 23: Valence spectra for free tin clusters at 0.00% O_2 (**a**)and 1.3% O_2 (**b**). In Spectrum **a** the metallic band is seen above 4 eV. This metallic band is also noted for spectrum **b** between 4 eV and 6 eV.

In figure 23, spectrum **a**, the band structure for the metallic case can be seen. In spectrum **b** this band may still be seen between 4 eV and 6 eV, though the spectrum has become dominated by the oxide component. In figure 24 it can be seen that from spectrum **c** onwards no contribution from the metallic tin is present. The spectrum presents as two distinct components: one between 6 eV and 8 eV, the second from 8 eV to 14 eV. Increasing the oxygen concentration in the beam led to the disappearance of the 6 $eV - 8$ eV component. The peak present in the 8 $eV - 14$ eV component shifted towards higher energies as the oxygen concentration increased, similar to the case for the $4d$ level mentioned earlier.

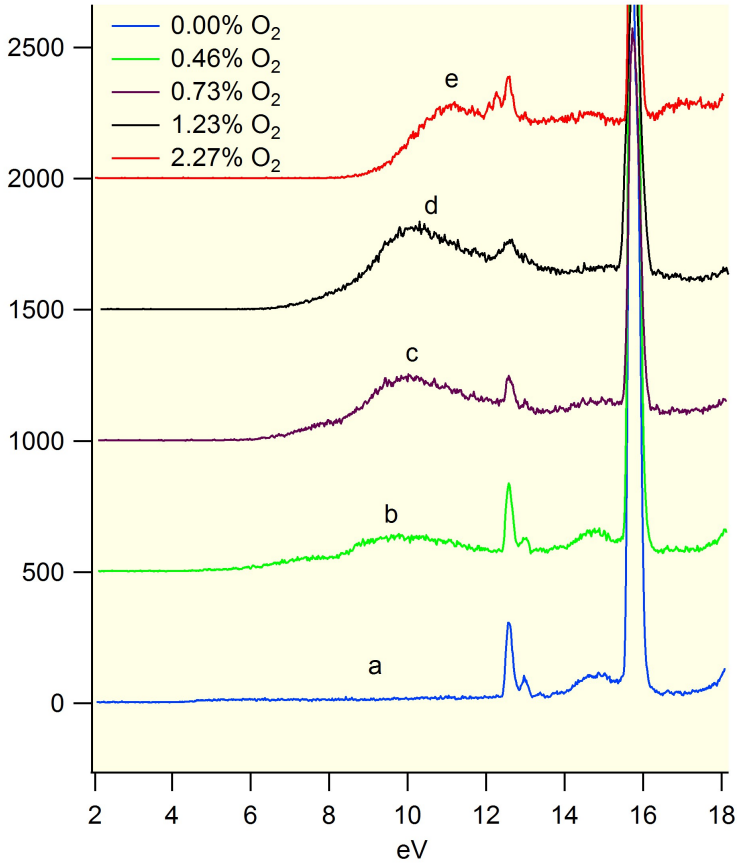

Figure 24: Tin of various O_2. Valence spectra at various O_2 concentrations. The dominant peak near 16 eV is the argon $3p$ line to which the spectra were calibrated.

The 4 $eV - 6$ eV component disappears in later spectra though tin (IV) oxide has not yet become established. This suggests that the valence spectra can indicate the presence of tin oxides but due to the smooth progression as intermediate oxides occur cannot be used as an indicator as to the dominance of tin (II) oxide or tin (IV) oxide.

6.2.2 Deposited Clusters of Tin and Tin Oxide

Clusters were formed in the beam and the oxygen concentration adjusted to facilitate the production of tin (II) oxide or tin (IV) oxide as required. The oxidation state was confirmed by collecting spectra of the free clusters prior to deposition on the silicon substrate. Deposited clusters were characterised by observing the Sn $4d$ and Sn $3d$ levels. The Sn $3d$ level having become accessible due to the greater density of deposited particles in the volume irradiated than was the case for free clusters.

The Sn $3d$ level, collected at 600 eV,for deposited tin (II) oxide and tin (IV) oxide is illustrated in figure 25. Spectrum **a** is for tin (II) oxide and also contains a weak doublet towards the lower binding energy side of the tin (II) oxide doublet. After fitting, the shift from metallic tin to tin (II) oxide is found to be 1.6 eV compared to the 1.3 eV for the case of the Sn $3d$ in free clusters. This higher value may be attributed to the presence of small amounts of intermediate oxides which could have formed on the sample during or after deposition. The broad peaks present in the spectrum could easily be composed of unresolved closely overlapping peaks.

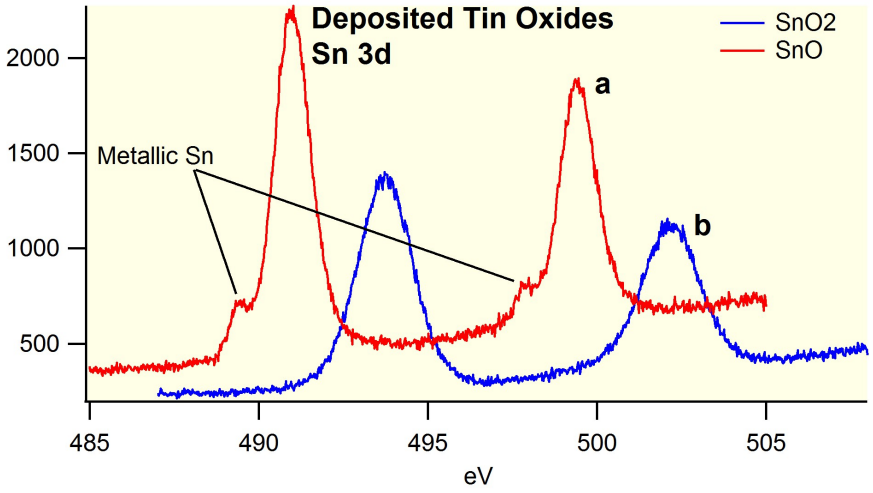

Figure 25: Sn $3d$ spectra for tin (II) oxide and tin (IV) oxide, presented as recorded.

To accurately determine the shift between metallic tin and tin (IV) oxide it is necessary to calibrate both spectra. In the case of spectrum **a** this can be done by adding the work function to the fitted peak positions, which are recorded relative to the zero energy point of the electron spectrometer. For spectrum **b** however this is not possible. Taken without calibration the shift between metallic tin and tin (IV) oxide is found to be 4.3 eV compared to the 4.2 eV for free clusters. This small shift may be due to charging of the sample due to the ejection of multiple electrons as a result of the sample irradiation by x-rays. Since the sample is a semiconductor this charge builds up on the sample, thus shifting the binding energy.

The Sn $4d$ spectra are illustrated in figure 26. For the tin (II) oxide case (spectrum **a)** the presence of a weak separate peak towards lower binding energies is observed which is not present in the tin (IV) oxide spectrum (spectrum **b**). Comparison with the spectra recorded for the free tin clusters and considering the close proximity of the peak to that for the free metallic clusters, this peak has been assigned to that of metallic Sn $4d_{5/2}$. The complex shape of the peak has thwarted attempts at an accurate fitting, though the presence of two equal intensity maxima cannot be described by a single doublet due

to the spin-orbit splitting ratio of d orbitals being 2:3. This suggests the presence of multiple oxide states (at least two) in addition to small quantities of metallic tin. The dominant peak in spectrum **b** can be fit with a single doublet and based upon its position and through comparison with the free cluster spectra is assigned to the tin (IV) oxide response.

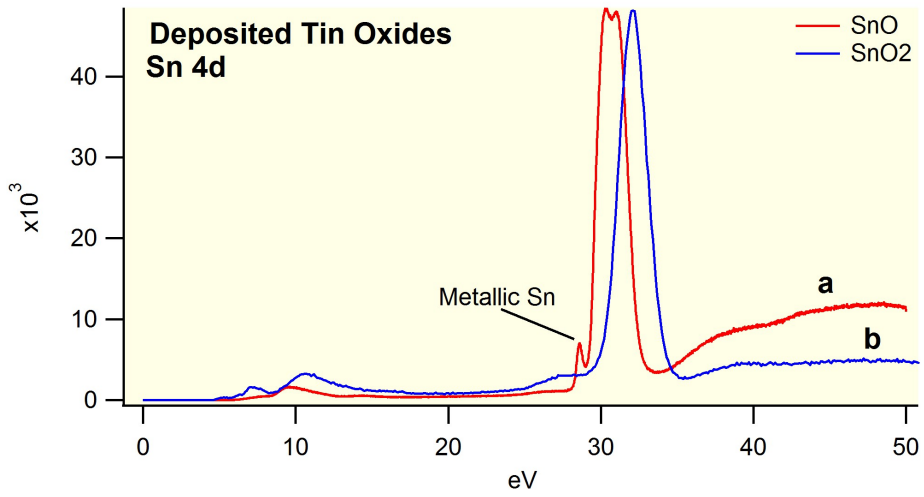

Figure 26: *Sn 4d* spectra for tin (II) oxide and tin (IV) oxide, presented as recorded. Spectrum **a** was gathered at 100.2 eV while spectrum **b** was gathered at 215 eV.

To determine the size of clusters for tin (II) oxide and tin (IV) oxide SEM images of the deposited clusters were taken, since the semiconducting nature of the oxides prohibits the use of the conducting sphere model. Figure 27a illustrates the SEM image taken for the tin (II) oxide while figure 27b illustrates that for tin (IV) oxide. Both SEM images are of the edge of the deposition area where deposition is less dense and individual clusters are more easily distinguished. For the case of tin (II) oxide the dominant cluster size is seen to be approximately 10 nm. For tin (IV) oxide however, there appears have been a greater degree of agglomeration on the substrate and it is more challenging to separate individual clusters. Nevertheless a particle size of $10 - 20$ nm is estimated.

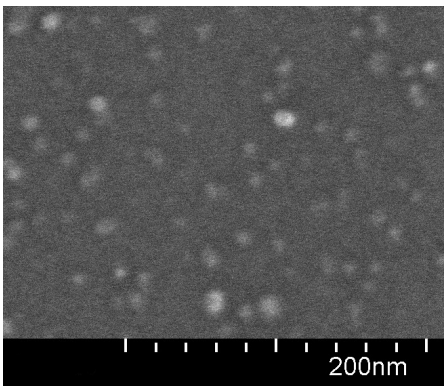

(a) SEM image of tin (II) oxide taken at the edge of the deposition area. The typical size of the deposited clusters is ≈ 10 nm.

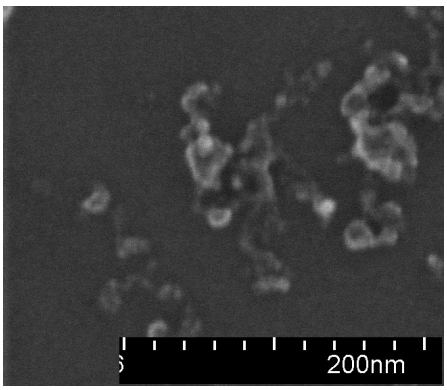

(b) SEM image of tin (IV) oxide taken at the edge of the deposition area. The typical size of the clusters is $\approx 10 - 20$ nm.

Figure 27: SEM images of deposited tin/tin oxide clusters.

7 Conclusions

The photoelectron experiments on free gold and silver clusters, picking up bromobenzene molecules have allowed us to shed additional light on the details of bromobenzene adsorption which are relevant for important and sophisticated catalytic process. This has been possible to do in the absence of any substrate which could obscure or modify the inherent interaction between the clusters and organic molecules.

Previously, the chemical shift between tin and tin (IV) oxide has been quoted as 2.0 eV [1], far less than for its neighbouring elements, lead and germanium. The experiments discussed in this thesis determine the shift to be 4.2 eV. It is proposed that this discrepancy is the result of a failure to sufficiently oxidise the tin-foil sample in order to create tin (IV) oxide. The possibility to create nanoscale tin oxide of controlled composition is important for the current activities in the field of large-gap transparent semiconductors.

The results in this thesis also demonstrate the potential when using a method of producing free clusters in a beam to modify the tin-oxidation degree on the fly and to characterise it using x-ray photoelectron spectroscopy.

8 Outlook

The continuation of the gold/silver experiments can be seen in an attempt to deposit clusters with adsorbed molecules, expose them to the other ingredient of a Sonagashira catalytic reaction and then control the resulting products using a mass-spectrometer.

For tin oxide clusters one could make an attempt to deposit clusters on transparent substrates and measure their absorption spectrum in the infrared, visual, and UV regions. That can in principle permit one to establish the band gap of the clusters, and thus complement the results of the photoelectron spectroscopy study. The band-gap is important for the potential applications as nanoscale semiconductor objects.

References

[1] P De Padova, M Fanfoni, R Larciprete, M Mangiantini, S Priori, and P Perfetti. *Surf Sci*, 313(3):379–391, 1994.

[2] Roy L. Johnston. *Atomic and Molecular Clusters*. 1st edition, 2002.

[3] Ezequiel Pedro Marcos Leiva (auth.) Marcelo Mario Mariscal, Oscar Alejandro Oviedo. *Metal Clusters and Nanoalloys: From Modeling to Applications*. Nanostructure Science and Technology. Springer-Verlag New York, 1 edition, 2013.

[4] Professor Dr. Hellmut Haberland (eds.) R. S. Berry, H. Haberland (auth.). *Clusters of Atoms and Molecules: Theory, Experiment, and Clusters of Atoms*. Springer Series in Chemical Physics 52. Springer-Verlag Berlin Heidelberg, 1 edition, 1994.

[5] O Björneholm, G Öhrwall, and M Tchaplyguine. *Nucl Instrum Meth A*, 601(1): 161–181, 2009.

[6] Yasushi Nishihara (eds.) Yaushi Nishihara (auth.). *Applied Cross-Coupling Reactions*. Springer-Verlag Berlin Heidelberg, 1 edition, 2013.

[7] G.J. Szulczewski and J.M. White. *Surf. Sci*, 399(2):305–315, 1998.

[8] D. Syomin and B. E. Koel. *Surf. Sci*, 490(3):265–273, 2001.

[9] A. Corma, R. Juárez, M. Boronat, F. Sánchez, M. Iglesias, and H. García. *Chem. Commun*, 47(5):1446–1448, 2011.

[10] V. K. Kanuru, G. Kyriakou, S. K. Beaumont, A. C. Papageorgiou, D. J. Watson, and R. M. Lambert. *J. Am. Chem. Soc*, 132(23):8081–8086, 2010.

[11] Yong Qiang He, Na Na Zhang, Yu Liu, Jian Ping Gao, Mao Cong Yi, Qiao Juan Gong, and Hai Xia Qiu. *Chinese. Chem. Lett*, 23(1):41 – 44, 2012.

[12] M. Ciobanu, B. Cojocaru, C. Teodorescu, F. Vasiliu, S.M. Coman, W. Leitner, and V.I. Parvulescu. *J. Catal*, 296:43–54, 2012.

[13] Yuta Matsushima, Yukie Nemoto, Tsutomu Yamazaki, Kazuyuki Maeda, and Takeyuki Suzuki. *Sensors Actuat B-Chem*, 96(1):133–138, 2003.

[14] Xiaofeng Wang, Hongwei Qin, Yanping Chen, and Jifan Hu. *J Phys Chem C*, 118 (49):28548–28561, 2014.

[15] M. Batzill and U. Diebold. *Prog. Surf. Sci*, 79(2):47–154, 2005.

[16] K Siegbahn, C Nordling, A Fahlman, R Nordberg, K Hamrin, J Hedman, G Johansson, T Bergmark, SE Karlsson, I Lindgren, et al. *Almqvist, Wiksells, Stockholm*, pages 1994–1995, 1967.

[17] A. Jablonski and C.J. Powell. *J Electron Spectrosc*, 100(1):137–160, 1999.

[18] Associate Professor D. John O'Connor Dr. Brett A. Sexton Professor Roger St. C. Smart (eds.) C. Klauber, R. St. C. Smart. *Surface Analysis Methods in Materials Science*, volume 23. Springer-Verlag Berlin Heidelberg, 2 edition, 2003.

[19] Hans Lüth. *Solid Surfaces, Interfaces and Thin Films*. Springer Berlin Heidelberg, 5th ed. edition, 2010.

[20] M.P. Seah and W.A. Dench. *Surf. Interface. Anal*, 1(1):2–11, 1979.

[21] Willmott P. *An Introduction to Synchrotron Radiation*. Wiley, 2011.

[22] John David Jackson. *Classical electrodynamics*. Wiley, 3rd ed edition, 1999.

[23] M Bässler, A Ausmees, Marko Jurvansuu, R Feifel, J-O Forsell, P de Tarso Fonseca, A Kivimäki, S Sundin, SL Sorensen, R Nyholm, et al. *Nucl. Instrum. Meth. A*, 469 (3):382–393, 2001.

[24] A. Puschmann C. Xue D.A. Shirley G. Kaindl H. Petersen P. Kuske M. Domke, T. Mandel. *Rev. Sci. Instrum*, 63(1):80–89, 1992.

[25] Volker Schmidt. *Electron Spectrometry of Atoms using Synchrotron Radiation*. Cambridge University Press, 2005.

[26] Chris Binns. *Nanomagnetism : fundamentals and applications*. Frontiers of nanoscience. Elsevier Science, 2014.

[27] R. Behrisch. *Sputtering by Particle Bombardment I: Physics and Applications*. Topics in applied physics. Springer-Verlag, 1981.

[28] Stephen M Rossnagel. *IBM. J. Res. Dev*, 43(1.2):163–179, 1999.

[29] Shigeru Haber Kiyotaka Wasa. *Handbook of Sputter Deposition Technology: Principles, Technology and Applications (Materials Science and Process Technology Series)*. Noyes Publications, 1992.

[30] JJ Yeh and I Lindau. *Atom. Data. Nucl. Data.*, 32(1):1–155, 1985.

[31] Terrance E Conners and Sujit Banerjee. *Surface analysis of paper*. CRC Press, 1995.

[32] E Kukk. Spectral analysis by curve fitting macro package/spancf/2000. *See www. physics. utu. fi/en/department/materials_ research/materials_ science/Fitting. html for details of the lcode used to carry out the least-squares fit of the experimental data.*

[33] Timothy J Drummond. Work functions of the transition metals and metal silicides. Technical report, Sandia National Labs., Albuquerque, NM (US); Sandia National Labs., Livermore, CA (US), 1999.

[34] Herbert B Michaelson. *J. Appl. Phys*, 48(11):4729–4733, 1977.

[35] A Kivimäki, SL Sorensen, M Tchaplyguine, M Gisselbrecht, RRT Marinho, Reimund Feifel, Gunnar Öhrwall, Svante Svensson, and Olle Björneholm. *Phys. Rev. A*, 71(3): 033204, 2005.

[36] Nguyen Tri Khoa, Soon Wook Kim, Dae-Hwang Yoo, Eui Jung Kim, and Sung Hong Hahn. *Appl. Catal. A-Gen*, 469:159–164, 2014.

[37] M. Tchaplyguine, G. Öhrwall, T Andersson, S. Svensson, O. Björneholm, M Huttula, M Mikkelä, S. Urpelainen, S Osmekhin, A Caló, et al. *J. Electron. Spectrosc*, 195: 55–61, 2014.

[38] Toshiaki Ohta, Takashi Fujikawa, and Haruo Kuroda. *B. Chem. Soc. Jpn*, 48(7): 2017–2024, 1975.

[39] Elettra. *Atomic Calculation of Photoionization Cross-Sections and Asymmetry Parameters*, 2016. https://vuo.elettra.eu/services/elements/WebElements.html [Accessed: 07/04/2016].

[40] Mattis Fondell, Mihaela Gorgoi, Mats Boman, and Andreas Lindblad. *J. Electron. Spectrosc*, 195:195–199, 2014.

[41] BB Alchagirov, OI Kurshev, TM Taova, and Kh B Khokonov. *Tech. Phys+*, 51(12): 1624–1626, 2006.

[42] SK Gupta, AK Kapil, CM Singal, and VK Srivastava. *J. Appl. Phys*, 50(4):2852–2855, 1979.

[43] GK Wertheim and DNE Buchanan. *Solid. State. Commun*, 69(6):689–692, 1989.